Composites Part B 316 (2026) 113580

Contents lists available at ScienceDirect

Composites Part B

journal homepage: www.elsevier.com/locate/composites

Investigation of permeability and leakage in composite materials for application in cryogenic storage systems

J. Koord [a,*], H. Kumazawa [b], A. Fischer [c], T. Ebina [d], O. Völkerink [e], C. Hühne [a,e]

[a] German Aerospace Center (DLR), Institute of Lightweight Systems, Lilienthalplatz 7, 38108 Braunschweig, Germany
[b] Japan Aerospace Exploration Agency (JAXA), Aviation Technology Directorate, 6-13-1 Ohsawa, Mitaka-shi, Tokyo, 181-0015, Japan
[c] German Aerospace Center (DLR), Institute of Space Systems, Robert-Hooke-Str. 7, 28359 Bremen, Germany
[d] National Institute of Advanced Industrial Science and Technology (AIST), 4-2-1 Nigatake, Miyagino-ku, Sendai, 983-8551, Japan
[e] Technische Universität Braunschweig, Institute of Mechanics and Adaptronics (IMA), Langer Kamp 6, 38108 Braunschweig, Germany

ARTICLE INFO

Keywords:
Composites
Permeability
Barrier
Leakage
Cryogenics
Microcracks
Biaxiality

ABSTRACT

Liquid hydrogen storage systems made from composite materials offer promising advantages for future lightweight aircraft. However, to ensure functionality and safety, these tanks must exhibit both low hydrogen permeability and high resistance to microcrack formation — especially under cryogenic conditions. Testing either of these parameters is not straightforward. In the present work, different test setups are employed to quantify permeability and leakage, and to differentiate between these two phenomena. Pragmatic approaches for elevated, room and low temperature permeability testing are presented, including a direct comparison of helium and hydrogen permeability, and permeability values down to cryogenic temperatures are provided. Permeability at 77 K and 20 K is estimated through regression-based extrapolation of experimental temperature-dependent permeability data. In addition, the effectiveness of clay-based barrier materials in further reducing gas permeation is quantified. Regarding leakage, the limitations of unidirectional thermo-mechanical loading with respect to crack network formation are demonstrated. By applying biaxial loading, crack networks are introduced and the temperature- and pressure-dependence of gas flow through these networks is analyzed. The presented methodology and results offer practical tools for material evaluation and support the design of composite structures for cryogenic hydrogen storage.

1. Introduction

In recent years, much effort has been dedicated to developing sustainable aircraft concepts to mitigate aviation's impact on global climate. Among these concepts, hydrogen-powered aircraft represent a promising solution for reducing emissions [1–3]. However, transitioning to hydrogen power requires a comprehensive redesign of the aircraft's propulsion and energy storage system. Unlike traditional kerosene-based aircraft, where fuel is primarily stored in the wings, hydrogen storage currently presents a great challenge for future aircraft.

Due to the inefficiency of storing hydrogen in gaseous form, in terms of energy density per unit mass (gravimetric) and energy density per unit volume (volumetric), this option is unattractive for most aircraft configurations [4,5]. Liquid hydrogen storage at 20 K offers advantages in both volumetric and gravimetric storage indices compared to gaseous storage. However, compared to kerosene, liquid hydrogen still occupies roughly four times the volume at about one-third of the weight for equal energy levels [6]. Considering the fuel alone, liquid hydrogen storage requires a larger volume but weighs less. As a result, and while considering weight distribution and optimal space utilization, the most promising concepts involve storing hydrogen within the fuselage [7], see Fig. 1. As hydrogen storage is associated with large volumes but low fuel mass, the mass of the storage system, i.e. structure and systems, plays a significant role in the overall mass analysis. Herein, development of storage systems made of CFRP as opposed to aluminum promises a reduction in structural weight of about 30 % and a reduction in manufacturing cost of about 25% [8].

Appropriate thermal insulation is crucial for minimizing boil-off, which enables efficient storage and thereby ensures acceptable range in flight as well as dormancy times on the ground. Rather simple insulation concepts, such as foam insulation used in space launcher systems, prove inadequate to meet boil-off requirements. Instead, a double-walled tank with ultra vacuum combined with a multi-layer insulation (MLI), is frequently considered in literature [9] (see Fig. 1). While vacuum reduces convective heat transfer, MLI suppresses radiation. For this insulation concept to work effectively, the vacuum

* Corresponding author.
E-mail address: josef.koord@dlr.de (J. Koord).

https://doi.org/10.1016/j.compositesb.2026.113580
Received 16 October 2025; Received in revised form 16 February 2026; Accepted 3 March 2026
Available online 4 March 2026

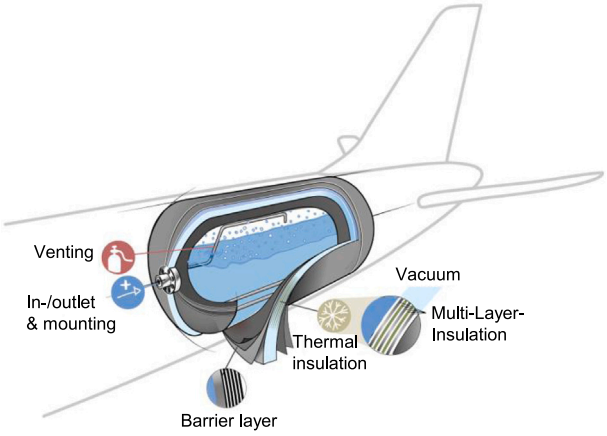

Fig. 1. Schematic CFRP hydrogen tank concept for aviation.

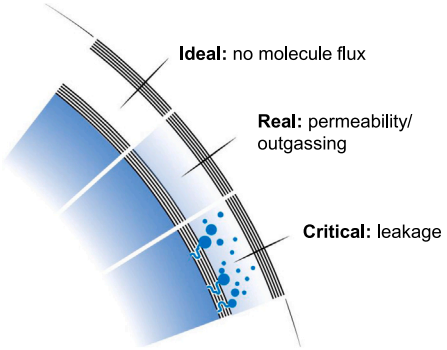

Fig. 2. Schematic representation of molecular flux into the vacuum insulation from the inside (permeability and leakage) and the outside of the tank wall (outgassing)

needs to be maintained continuously. However, due to hydrogen permeation through the inner tank wall as well as outgassing through the outer tank wall (see Fig. 2), molecules can continuously enter into the insulation and potentially degrade the pressure level, thereby compromising insulation efficiency.

While permeability influences insulation efficiency and, consequently, aircraft range and dormancy time, leakage presents a safety concern and must be avoided at all times. As opposed to permeability, which progresses at a comparatively gradual pace, leakage entails a rapid molecular flow through a network of cracks within the CFRP structure. This accelerated flow has the potential to swiftly compromise insulation integrity and even lead to catastrophic structural failure in case of sudden expansion of large amounts of liquid hydrogen, resulting in a significant pressure increase. A prominent example case is the failure of the NASA X-33 composite cryogenic hydrogen tank in the early 2000s [10], which is often referenced in literature.

As a multiphase material, CFRP consists of layers of fibers oriented in various directions and resin, each component possessing distinct thermal expansion coefficients. Cooling of CFRP down to cryogenic temperatures results in thermal residual stresses building up, consequently promoting crack initiation and propagation [11]. Additionally, mechanical loading, such as the storage pressure, aggravates stress levels, thereby potentially accelerating the formation of crack networks. Due to the fact that CFRP is (i) susceptible to the formation of microcracks and (ii) diffusion of hydrogen molecules in CFRP occurs at higher rates compared to metals, permeability and leakage require special care during CFRP hydrogen tank development.

When discussing the effects of microcracks on permeability and leakage, special care must be taken in defining these phenomena. As permeability and leakage are used interchangeably in many publications, Fig. 3 is intended to differentiate permeability and leakage: The diffusion-based flux of molecules through pristine CFRP material, as shown in Fig. 3(a), is defined as permeation, and the corresponding material property is permeability. As discussed in the previous section, composite materials can develop microcracks. However, the presence of isolated cracks in a composite does not significantly affect the material's permeability (cf. Fig. 3(b)). Typically, the difference in permeability between a pristine specimen and one with isolated cracks cannot be quantified using state-of-the-art testing methods [12–15], out of which mass spectrometry-based leak detectors have the highest sensitivity ($\sim 10^{-12}$ mbar l/s). Publications that suggest otherwise often lack a physical explanation as to why permeability measured on a global level would increase with an increasing crack density [16] or they are actually referring to molecular flux through crack networks (leakage) as permeation [17–19]. Once the crack density reaches a threshold where an interconnected crack network forms, as is the case in Fig. 3(c), thereby providing a continuous path through the thickness of the specimen, leakage becomes the dominant mechanism of gas transport. Unlike permeation, leakage is based on molecular flow, resulting in a flux that is by orders of magnitude higher than permeability.

In order to better differentiate and build a broader understanding, the present paper provides a comprehensive investigation into the key factors influencing permeability and leakage in composite materials. The main objectives of this study are to:

- Offer insights into the primary dependencies of permeability on variables such as tracer gas, pressure, specimen geometry, and testing conditions.
- Provide pragmatic recommendations for improving the reliability and reproducibility of permeability measurements across various experimental setups.
- Propose a methodology for estimating permeability at cryogenic temperatures, overcoming limitations in state-of-the-art testing infrastructure.
- Differentiate between true material permeability, leakage effects, and the influence of test setups and loading history on measurement outcomes.

By addressing these objectives, this study aims to enhance the understanding of composite permeability behavior and improve experimental techniques, ultimately supporting the development of more robust and reliable composite material systems.

2. Literature study

A brief literature study on the main influencing factors of permeability and leakage is given in the following.

2.1. Tracer gas

In past years, hydrogen permeability under cryogenic conditions was mainly investigated in the context of cryogenic tank development for space application. Despite hydrogen permeability being the property of interest, many studies focus on helium as tracer gas. On the one hand, helium is an inert gas and therefore safer to handle than hydrogen, which at concentrations above 4% and 18% is flammable and explosive, respectively. On the other hand, leak detectors have a better sensitivity measuring helium compared to hydrogen due to the increased background noise when using hydrogen [20,21]. Comparability of hydrogen and helium permeability in composites has been investigated mainly by Humpenöder [22] and Schultheiß [14]. At room temperature, hydrogen permeability ($4.5 \cdot 10^{-13}$ m^2/s) through CFRP is slightly larger than helium permeability ($4.0 \cdot 10^{-13}$ m^2/s) [22]. Humpenöder [22] further investigates a temperature range between 230 K (−43 °C) and room temperature and finds the difference between

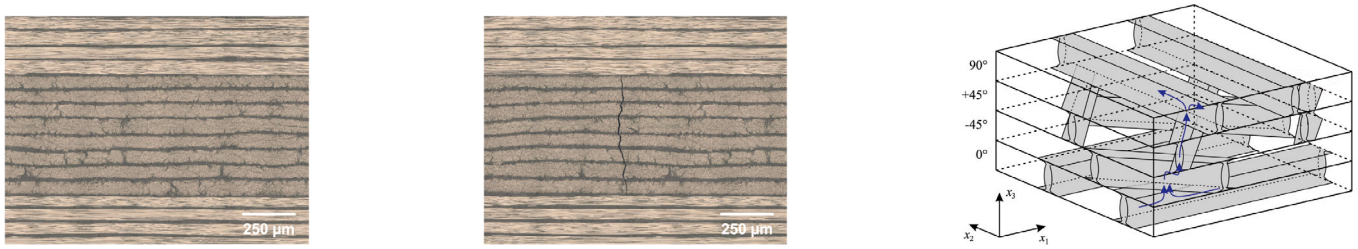

(a) Pristine material (b) Isolated crack (c) Crack-network [23]

Fig. 3. Differentiation between (a) permeability in pristine CFRP and (b) in CFRP with isolated crack versus (c) leakage in CFRP with inter-connected cracks (crack-network)

helium and hydrogen permeability to be well below one order of magnitude. Results by Schultheiß [14] for different types of CFRP indicate that helium permeability is larger by a factor of 1.1–8. The results show that helium and hydrogen permeability are in general comparable taking into account the relatively large uncertainty of the testing methods (±15–30%). However, more studies are needed especially in the cryogenic regime to confirm those results. Nonetheless, as helium is the only element of comparable molecular size to hydrogen, there is no viable alternative in terms of tracer gas for permeability testing.

A direct quantitative comparison of permeability data obtained with different test gases is generally limited, as reported values are strongly influenced by testing conditions, in particular temperature, and by the material system. In CFRP, gas permeability depends on resin type, fiber volume fraction (FVF), laminate quality, and specimen condition. Consequently, literature data obtained using helium or hydrogen may differ by up to an order of magnitude even for nominally similar materials [24]. When interpreted in the context of their respective material systems and testing conditions, the permeability data reported here, as well as those reported by Humpenöder and Schultheiß, are therefore comparable on an order-of-magnitude level rather than through a direct numerical conversion.

2.2. Testing pressure and temperature

Apart from the tracer gas, testing pressure and testing temperature are parameters to select during permeability testing. Flanagan [19] investigates pressures between 1 bar and 10 bar at room temperature and finds permeability to be constant. Similar results are reported repeatedly in literature [14,22]. Regarding the effect of temperature, more studies are present: Humpenöder [13,22] reports the permeability of CFRP, GFRP and pure resin to follow the Arrhenius relation.[1] Due to the exponential decrease in permeability with decreasing temperature, the test results are limited to a lower testing temperature of 200 K since the test setup is not able to resolve permeabilities below 10^{-15} m^2/s. The activation energy that describes the temperature dependency is 20 kJ/mol for CFRP. Disdier et al. [12] investigate permeability in the temperature range between 260 K to 350 K. Similar observations regarding temperature dependency are made. Test data by Schultheiß [14] confirms the previous observations for a temperature range between −50 °C (223 K) and 50 °C (323 K). The calculated activation energies for different CFRP specimens range between 15–20 kJ/mol. A recent study by Katsivalis [25] further confirms the applicability of the Arrhenius relation to the temperature dependency of hydrogen permeability in CFRP for temperatures between 5 °C (278 K) and 45 °C (318 K). While the literature agrees on the general applicability of the Arrhenius relation for describing the temperature dependency of permeability in CFRP, test results for temperatures below 200 K (−73 °C) are not available to confirm the assumption for the cryogenic regime.

2.3. Materials

Considering different types of composite materials, the difference in permeability usually ranges below one order of magnitude [19]. Rather than the type of composite, e.g. GFRP vs. CFRP, the FVF has a more significant influence on permeability. Therein, permeability is observed to decrease with increasing FVF [12,19,22,26]. Permeability reduces by roughly one order of magnitude for FVF between 24% and 65% [12]. The main reason being the fibers acting as obstacles and reducing the effective volume for diffusion within a specimen. A similar effect can be achieved by adding fillers: Timmerman et al. [27] achieve a reduction in permeability by 70% through dispersion of 2 wt.% nano-particles of clay into the matrix. By adding nano-flakes made of glass into epoxy resin, van Rooyen et al. [28] report a reduction in permeability by three orders of magnitude. In both cases, the orientation of the nano-fillers is of great importance as the underlying mechanism for reduction of permeability is the increase of diffusion path length combined with a decrease in effective diffusion cross-section. While fillers represent a material modification and do not significantly influence the manufacturing process, applying barriers, i.e. a liner, with low permeability is yet another concept to reduce permeability [29,30]. A large number of studies is present on this topic. While metallic liners and plastic liners with additives promise a permeability reduction as well as an additional safety layer in case of leakage through crack networks in a composite, applying a liner of any kind complicates the manufacturing process of a tank structure and adds mass which both is undesirable.

Up to this point, the literature study focused on permeability in pristine composite material, the following section shall give a brief overview on influencing parameters in non-pristine, i.e. laminates containing microcracks. Permeability/leakage tests are often combined with microcrack analysis, as microcracks are typically the cause of leaks. Microcracks may result from thermal stresses induced by cryogenic conditions, mechanical loads or combined thermo-mechanical loading. The vast majority of publications focus on only one type of stress (see review article by Saha et al. [24]), however, the combination of thermal and multi-axial mechanical loads represents the critical load case and can increase leak rates by several orders of magnitude [31]. This combined load case is especially relevant for tank applications.

2.4. Effect of thermal loading

Results on the impact of thermal cycling vary significantly [32]. While some studies show no change in leak rate through thermal cycling [12–14], others indicate that the molecular flux through a

[1] The Arrhenius relation explains how reaction rates speed up as temperature rises, due to the increased energy available to overcome activation barriers. It highlights the exponential nature of this temperature dependence and is widely used to model reactions and diffusion in materials. Essentially, it helps predict how quickly processes happen at different temperatures.

specimen changes through thermal cycling [17–19]. Disdier et al. [12] report that thermal cycling of GFRP (64,120/E-glass and TE630/E-glass) in liquid nitrogen does not alter helium permeability, although some cracks are introduced into the laminate. Choi and Sankar [18] conduct helium permeability testing at room temperature (RT) after thermal cycling CFRP (graphite/epoxy) specimens in liquid nitrogen. Permeability is reported to increase by 3–10% after 20 cycles. However, no inter-connected crack network is observed. Dreossi and Horvath [33] apply up to 5 thermal cycles in liquid hydrogen at 20 K to CFRP specimens, while helium permeability remains at Fick'ian behavior. Flanagan et al. [19] cycle CFRP specimens with thermoplastic matrix (PEEK/AS4 and PEEK/IM7) up to 30 times in liquid nitrogen. They report that helium permeability does not alter in specimens with no microcrack networks. However, optical microscopy reveals crack networks in specimen with elevated leak rates. The authors also report a shift in curve behavior from near-Fickian (permeability) to non-Fickian (leakage) in specimens with microcrack networks. Bechel et al. [34] demonstrate on cryogenically cycled CFRP (5250-4/IM7 and 977-2/IM7) specimen with varying layups that one intact layer without the presence of microcracks is sufficient to prevent leakage. Regarding the number of cryogenic cycles in LN_2, a saturation in leak rate after 1–5 cycles is reported by Choi and Sankar [18], who applied 20 cryogenic cycles. Bechel et al. [35] conduct 1250 cryogenic cycles 5250-4/IM7 and reported onset of leakage at around 400 cycles and no saturation until 1250 cycles. In contrast, Yonemoto et al. [36] observe no leakage for up to 100 cryogenic cycles but a sharp increase in hydrogen leak rate after 1000 cycles in CFRP (#380/CF). However, it should be noted that for high-performance materials with strong crack resistance, thermal cycling alone – even at high cycle numbers – typically does not induce crack networks.

2.5. Effect of mechanical loading

Disdier et al. [12] observe an increase in leak rate of a factor of 1.3 after uniaxially loading a GFRP specimen in tension to 84% of its failure load at 4.2 K. At RT however, uniaxial tensile loading does not alter the helium molecule flux. Likely, the absence of thermal loads in the RT case prevented the formation of a crack-network.)Grenoble and Gates [37] apply cyclic uniaxial mechanical loading (R=0.01) on CFRP specimens to up to 0.4% strain at 77 K. Hydrogen leak rates were measured at −191 °C (82 K) after 170,000 cycles (10^{-2} sccm)[2] and 400,000 cycles (10^{-1} sccm). Furthermore, hydrogen leak rates at −191 °C (82 K) increase for specimens at 0.4% tensile strain by one order of magnitude compared to unloaded specimens. It should be mentioned that permeability analysis of damaged specimens is not trivial. As described by Bechel et al. [17], surface cracks can bypass the sealing between specimen and test chamber. Through these channels, molecules of the tracer gas (hydrogen or helium) from the environment can influence the measurement if no preventive actions are taken to counteract this phenomenon (cf. Fig. 4). This effect is commonly observed across various permeability and leakage testing methods, however, it is most pronounced in tests conducted under mechanical loading conditions. Therefore, experimental test results should be considered with caution.

In general, uniaxial tensile loading of multidirectional laminates leads to transverse cracks in off-axis layers rather than those layers aligned parallel to the loading direction (0° plies) [38]. Therefore, Yokozeki et al. [39] apply a combination of loading cases. First, plates are loaded in 3-point bending in transverse direction. Subsequently, the plate is loaded in longitudinal tensile direction. This procedure has the purpose to introduce transverse cracks in all plies, facilitating the development of a crack network. It is concluded that the *thermal* effect of cryogenic conditions suppresses damage-induced gas leakage due to lower molecular kinetics, while the *mechanical* effect increases leak rates. Furthermore, the study concludes that leak rates of damaged CFRP laminates at 77 K are similar to that at RT, allowing for the estimation of gas leakage under cryogenic conditions based on RT leakage data from specimens with identical damage states.

[2] Standard Cubic Centimeters per Minute

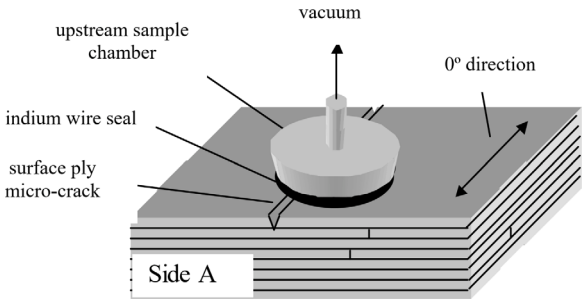

Fig. 4. Surface crack allowing gas to bypass seal between sample and test chamber [17].

Hamori et al. [40,41] apply biaxial loads to cruciform CFRP specimens at −253 °C (20 K). Subsequently, leak rates are measured at RT. To the best knowledge of the authors, in-situ leakage measurement on biaxially loaded specimens at cryogenic temperatures has not been reported in literature to date. Post-testing, biaxially loaded specimens exhibit cracks in all plies, resulting in leakage through crack networks. However, the formation of crack networks occurs at lower strain levels under cryogenic conditions. Furthermore, Hamori et al. show that thin-ply material can offset the formation of crack networks to higher strains.

Questioning the validity of previous testing due to the fact that studies have employed uniaxial loads and there has been no discussion or empirical evidence pertaining to how these loads relate to the biaxial state of stress in the material in its use environment (cryogenic composite tanks), Stokes [42,43] applies tetra-axial loads on bismaleimide-based multidirectional CFRP specimens. It is concluded that failure in the material initiates at the exposed surfaces and progresses towards the mid-plane. Localized failures can occur at strain levels as low as 1500 $\mu\varepsilon$, with widespread microcracking in the surface plies beginning between 2500 $\mu\varepsilon$ and 3000 $\mu\varepsilon$. Microcracking in the 0° plies starts between 3500 $\mu\varepsilon$ and 4000 $\mu\varepsilon$. The material exhibits some self-sealing behavior when unloaded, but once continuous surface-to-surface cracks form, they reopen at lower strain levels upon reloading. Leakage is identified as a time-dependent property influenced by strain. Catastrophic failure occurs above 4700 $\mu\varepsilon$. Although the stress states are not identical, the results are consistent with the findings of Hamori et al. [40,41] concerning the necessity of multi-axial loading for the formation of through-the-thickness crack networks in CFRP.

3. Experimental methods

3.1. Specimen manufacturing

Manufacturing of all specimens except for the biaxial specimens is done at German Aerospace Center (DLR). The specimens are fabricated using CFRP prepreg material (Hexcel HexPly 8552/35%/134gsm/IM7) with a cured ply thickness (CPT) of 0.125 mm. Multidirectional CFRP plates are manufactured by hand layup, vacuum sealed, and cured in an autoclave following the manufacturer's recommended curing cycle at 180 °C and 7 bar [44]. After the autoclave process, the specimens are cut to size by waterjet and measured using a micrometer. Specimens for permeability testing are round plates with 55 mm in diameter unless otherwise stated. Specimens for uniaxial tensile testing have a width of 70 mm and a length of 260 mm. Load-introduction tabs (70 × 50 mm) made of GFRP were bonded to the specimen ends using a

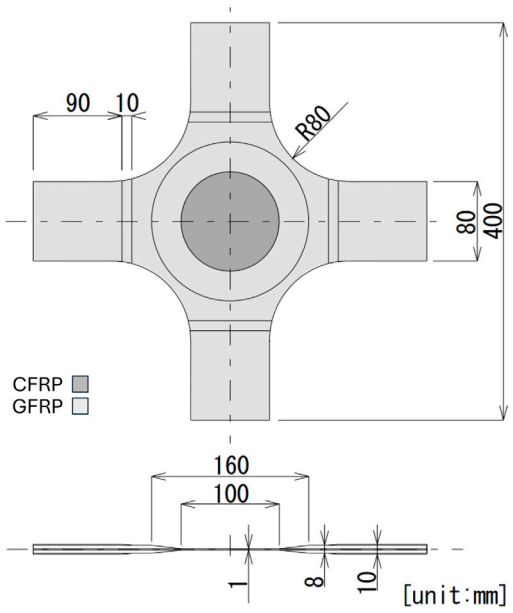

Fig. 5. Cruciform specimen geometry.

paste adhesive. Three layups are considered: unidirectional (UD) with a layup of $[0]_8$, a cross-ply (CP) with a layup of $[0,90]_{ns}$, and two quasi-isotropic (QI) with a layup of $[45,0,\text{-}45,90]_{ns}$ and $[45_2,0_2,\text{-}45_2,90_2]_{ns}$. The subscript s denotes a symmetric layup. Depending on the target specimen thickness, the number of repititions n is adjusted in accordance with the CPT. After manufacturing, the specimens are stored under ambient conditions unless otherwise stated. Void content was estimated from optical microscopy of polished cross-sections and was found to be well below 1%

Manufacturing of the biaxial specimens was conducted under the supervision of the Japan Aerospace Exploration Agency (JAXA). The biaxial specimens were fabricated by Super Resin, Inc. using UD CFRP prepreg with a curing temperature of 180 °C (HTA/#101) by Toho Tenax Co., Ltd. and National Electrical Manufacturers Association Standard G-10 GFRP. Two CFRP laminates with stacking sequences $[45_2,45_2]_s$ were manufactured, resulting in a specimen thickness of 1 mm. The geometry of the biaxial cruciform specimens is depicted in Fig. 5. The center of each GFRP tab was first tapered to a circular center hole with a diameter of 100 mm before bonding to both sides of the CFRP laminate. Tapering was done in order to prevent premature failure in the areas of high stress concentration in the cruciform specimen prior to the occurrence of leakage. Bonding was performed using an epoxy film adhesive L-134 (J.D. Lincoln Inc.) cured at 120 °C. The CFRP laminates with the bonded GFRP tabs were then machined into a cruciform shape.

3.2. Mechanical loading

The present section gives a brief overview on the test-rigs used for the present investigations. While the biaxial test-rig is situated at JAXA, the remaining test-rigs are all located at DLR.

3.2.1. Uniaxial mechanical loading

Uniaxial mechanical loading is conducted at DLR in a servo-mechanical testing machine by Zwick (Zwick 1478) equipped with a 100 kN load cell. The test procedure in terms of loading speed and test setup is based on ISO 527-5. However, it should be mentioned that the present specimen geometry and stacking sequence deviate from the recommendations in the standard. The specimen width of 70 mm is chosen to allow for permeability testing after mechanical loading. Strain gauges are applied on the surface of the mechanically loaded specimen for strain measurement.

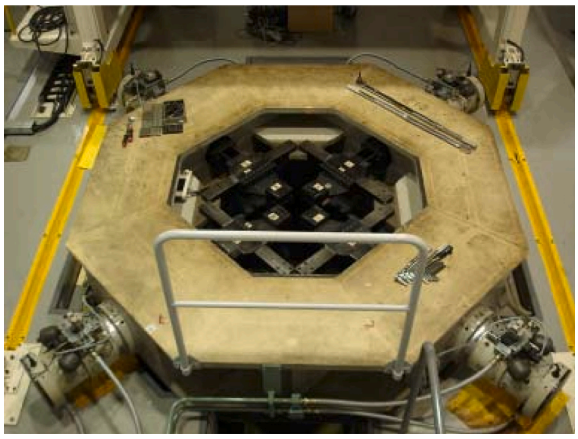

Fig. 6. Biaxial test-rig at JAXA.

3.2.2. Biaxial mechanical loading

In-plane biaxial tensile testing is conducted using a test-rig (cf. Fig. 6) at JAXA which consists of four hydraulic actuators with a load capacity of 245 kN (tension/compression). Four hydraulic actuators are arranged in two opposing pairs within a rigid, octagonal frame. The setup is positioned horizontally and is able to accommodate specimen of up to 1000 mm × 1000 mm in size. Hydraulic wedge grips secure the four arms of the cruciform specimens to the machine's crossheads, ensuring precise load application. A more detailed description of the test-rig and test conduction is provided in Kumazawa and Takatoya [45].

3.3. Thermal cycling

Thermal cycling refers to the immersion of CFRP specimens into LN_2. During immersion, direct contact of the specimens with LN_2 leads to a rapid cooling of the specimens down to 77 K. After a dwell time of 5 min the specimens are taken out of the LN_2 dewar and heated up under ambient air conditions. Once the specimen reach RT, they are immersed again until the target number of cycles is achieved. Temperature monitoring is done using thermocouples. The resulting average cooling and heating rates result to -13.3 ± 2.4 °C/min and 0.18 ± 0.03 °C/min, respectively.

3.4. Permeability testing

At DLR, different setups for permeability testing have been developed in recent years. While the setups are primarily developed to measure permeability (long testing times), they are also capable to capture leakage.

3.4.1. Testing at room temperature

Fig. 7 shows a test-rig for permeability testing at RT. The MSPT (multi-specimen permeability test) apparatus was developed in order to accelerate permeability testing [46], as testing time usually extends to several days until a steady state condition is reached. The test-rig consists of 6 cells that are connected in parallel. Each cell contains a specimen that is pressurized on the one side using helium as tracer gas. On the opposite side, the specimen is connected to a vacuum pump and leak detector (cf. Fig. 8). Each cell can be pressurized individually and connected to the leak detector individually to determine the helium flux. In the standard testing mode, the first cell is connected to the leak detector continuously to determine the permeability curve over time (usually several days). Once steady-state behavior is reached, the leak detector is connected to the remaining cells one-by-one to determine the plateau value (steady-state condition) for statistical purposes.

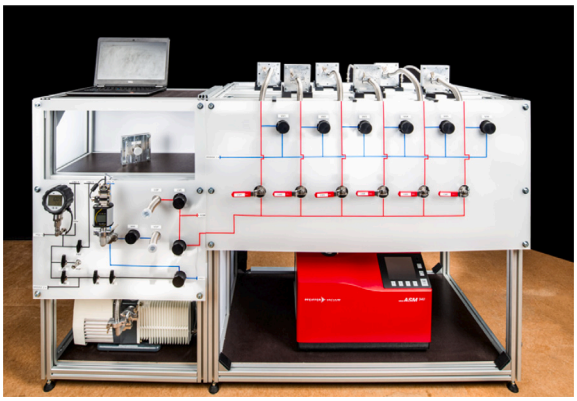

Fig. 7. Permeability test-rig for room temperature testing using helium.

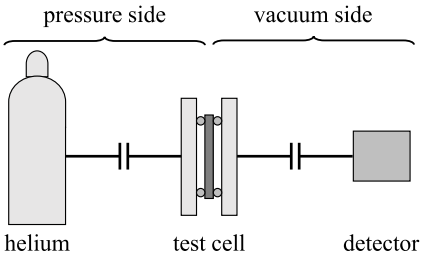

Fig. 8. Schematic setup for permeability testing.

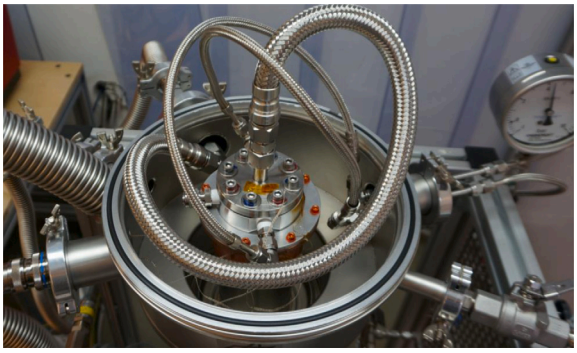

Fig. 9. Permeability test-rig for hydrogen testing.

During testing, helium pressure and temperature are monitored on the pressure side as well as vacuum levels and helium flux on the vacuum side of the setup.

The test-rig used for measuring hydrogen permeability, shown in Fig. 9, features a more complex design. Both helium and hydrogen fluxes can be measured using an ASM 340 leak detector by Pfeiffer Vacuum GmbH with an accuracy of ±15% according to the manufacturer's datasheet. Additional safety measures are implemented for hydrogen testing. The rig is operated in an explosion-proof laboratory and equipped with a ventilation system to prevent hydrogen accumulation. Prior to testing, the specimen is positioned at the center of the setup, sealed with indium, and clamped using eight bolts. The overall test configuration follows the schematic illustrated in Fig. 8, and the testing procedure is analogous to that of the MSPT setup, however, in the present case permeability is determined using hydrogen as tracer gas.

3.4.2. Testing in liquid nitrogen

In Fig. 10(a), a setup is presented for permeability testing under cryogenic conditions. The CIPT (cryogenic immersion permeability test) apparatus basically consists of a dewar container that is filled with LN_2. Analogous to the MSPT, a cell containing a specimen is immersed into the LN_2 bath and thereby cooled. The permeability test is conducted by pressurizing one side of the specimen helium as tracer gas, while the opposite side is connected to a leak detector.

Fig. 10. Setups for permeability testing in liquid nitrogen (CIPT) and in cold vapor phase (CVPT).

3.4.3. Testing in cold nitrogen vapor

In an attempt to determine permeability at temperatures between RT and 77 K, the setup in Fig. 10(b) was developed. In the CVPT (cold vapor permeability test) apparatus, the specimen is surrounded by the vapor phase of nitrogen. Depending on the LN_2 level with respect to the specimen cell, the temperature during testing can be controlled in an acceptable range ($\approx \pm 5$ °C) for several days. While nitrogen is used as cooling medium, permeability is determined using helium as tracer gas.

3.4.4. Data reduction method

Permeability P is derived post-testing from the helium flux $Q_L \left[\frac{\text{mbar l}}{\text{s}}\right]$, which is the output of the leak detector:

$$P = \underbrace{\frac{Q_L}{A}}_{q_L} \cdot \frac{d}{\Delta p} \cdot \frac{1}{R_m T} \qquad \left[\frac{\text{mol}}{\text{s m Pa}}\right] \tag{1}$$

The testing area A, the specimen thickness d, the pressure difference across the specimen Δp as well as the universal gas constant R_m and the temperature T serve as input.

4. Results and discussion

This manuscript follows a framework that distinguishes diffusion-dominated permeation in pristine material from damage-induced leakage through interconnected crack networks. HDPE is used as a reference polymer to establish gas-specific permeation behavior (He vs. H_2) under diffusion-dominated conditions. CFRP investigations then address (i) permeation trends in crack-free laminates and (ii) the transition to leakage under thermal, uniaxial, and biaxial loading scenarios representative of service-relevant stress states.

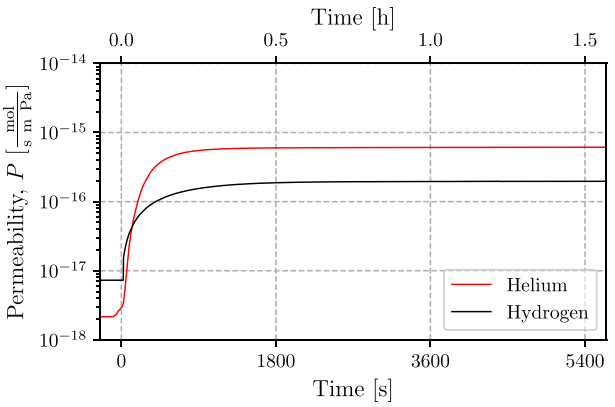

Fig. 11. Comparison of helium and hydrogen permeability in HDPE.

4.1. Permeability at room temperature

Room temperature testing is conducted using the permeability test-rig (MSPT) in Fig. 7.

4.1.1. Effect of tracer gas

In the vast majority of literature helium permeability is tested to address challenges of hydrogen storage [24]. A direct comparison between helium and hydrogen permeability is rarely provided. Humpenöder [22] introduces the following dependency of diffusivity of two gases as a function of their molecular size:

$$D_{\text{gas A}}/D_{\text{gas B}} = \exp(r_{\text{gas B}}/r_{\text{gas A}}) \tag{2}$$

With molecular sizes of 266 pm (He) and 276 pm (H_2), helium diffusivity is 2.8x higher than hydrogen diffusivity [14]. An experimental comparison by Humpenöder shows that helium diffusivity is higher by a factor of 1.6–6.6 compared to hydrogen. With permeability being a function of diffusivity D and solubility S ($P = D\ S$), experimentally determined values for helium permeability are generally slightly higher than hydrogen permeability, although usually by less than one order of magnitude [14,22,47].

To further add to this rather limited data, permeability tests were conducted. Identical specimens made of high-density polyethylene (HDPE, monomodal PE-300) were tested using helium and hydrogen, respectively. In between the tests, the specimen was stored in a vacuum chamber for 72 h to eliminate any residual gases in the specimens. After testing, the crystallinity of the specimen is determined by differential scanning calorimetry (DSC) using three samples with a diameter of 5 mm, resulting in a crystallinity of 61.6 ± 2.4%.

In Fig. 11, the permeability P is presented over the testing time. As can be seen, background noise and thus the minimum detectable leak rate is higher for hydrogen than it is for helium. The curve behavior, however, is very similar. Both specimens reach the steady-state condition after an initial steep transient increase. Therein, helium permeability ($6.02 \cdot 10^{-16}\ \frac{\text{mol}}{\text{s·m·Pa}}$) is higher by a factor of 3.1 than hydrogen permeability ($1.97 \cdot 10^{-16}\ \frac{\text{mol}}{\text{s m Pa}}$), which is in accordance with literature reportings [14,22,47]. It should be noted that both helium and hydrogen permeability in HDPE may vary with different composition and crystallinity of the polymer.

Although the permeability measurements on HDPE at room temperature provide $P_{\text{He}}/P_{\text{H}_2} \approx 3.1$, a quantitative transfer to CFRP is not generally justified because diffusivity and solubility of gases is polymer-specific. Any HDPE-based scaling for CFRP is therefore limited to a very rough estimate for pristine, diffusion-dominated material.

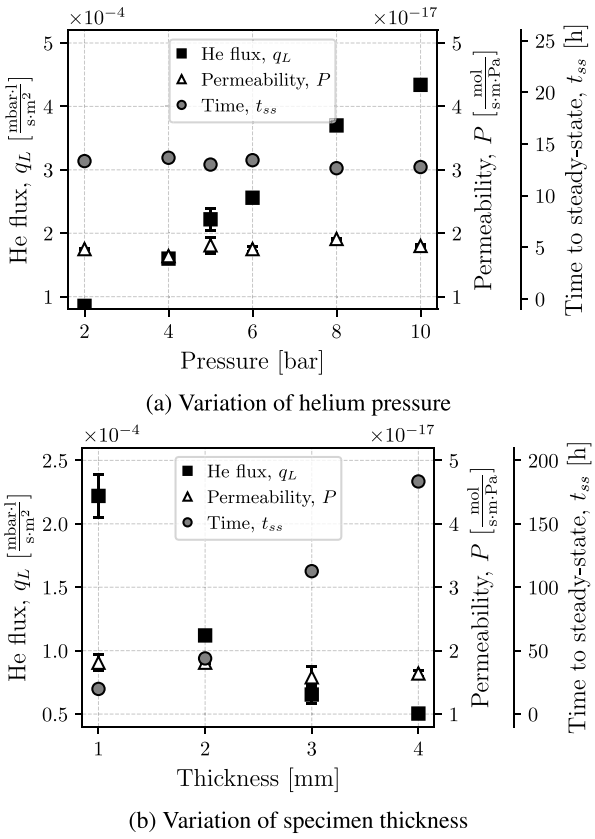

(a) Variation of helium pressure

(b) Variation of specimen thickness

Fig. 12. Effects of testing pressure and specimen thickness on permeability measurement.

4.1.2. Effect of testing pressure

In Fig. 12(a), the effect of varying pressure levels is investigated. The CFRP specimen has a CP layup with a thickness of 1 mm. A total of 5 testing configurations are run with a sample size of at least 3 for each pressure level, ranging from 2 bar to 10 bar. While the time until steady-state behavior t_{ss} is very similar for all pressure levels, it can be seen that the specific helium flux q_L increases with increasing pressure p_{He}. However, in terms of material permeability P the values are constant. Thus, for insulation system design where helium flux impacts performance, permeability can be measured at just one pressure and converted to a specific molecular flux. Further, it should be noted that above 10 bar, the ideal gas law no longer applies, potentially affecting adsorption on the pressure side and therefore permeability [14].

4.1.3. Effect of specimen thickness

Fig. 12(b) shows permeability P and helium flux q_L as a function of specimen thickness. The specimens exhibit a CP layup and are all tested at 5 bar. With increasing specimen thickness, testing time t_{ss} increases while the specific helium flux q_L decreases. Based on Fick's second law $J = -D\frac{\Delta C}{d}$ (with the flux J, diffusivity D and the concentration difference ΔC over a distance d) this result is expected, as the helium molecules travel a larger distance at otherwise constant pressure levels, and therefore helium concentrations on the pressure and vacuum side, respectively. For practical purposes, permeability can be measured using thin specimens and subsequently scaled to estimate the helium flux in thicker tank walls during system design.

4.1.4. Effect of laminate layup and specimen conditioning

While scaling of test results based on the testing conditions is demonstrated in the previous paragraphs, the question arises to what extent the characteristics of the specimen itself affects permeability

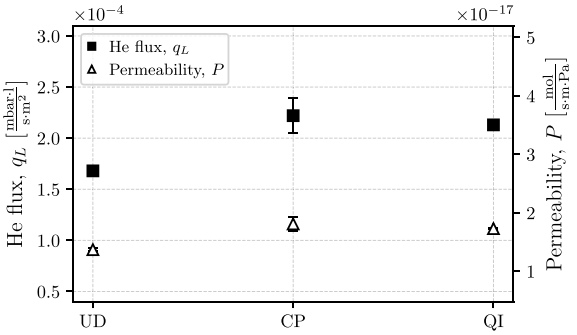

(a) Variation of specimen layup

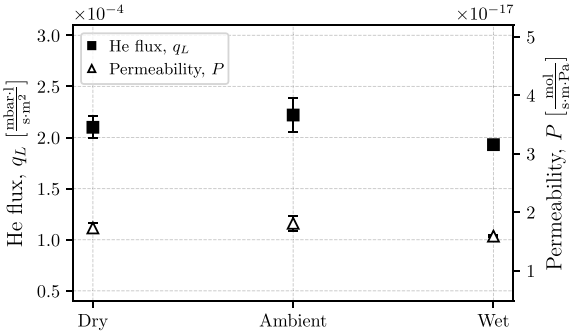

(b) Variation of storing conditions prior to testing

Fig. 13. Effects of specimen layup and pre-conditioning on permeability measurement.

measurement. For practical applications, the effects of varying layups and specimen conditioning are relevant. Testing is conducted at 5 bar pressure and 1 mm specimen thickness. The results are displayed in ascending order of laminate isotropy in Fig. 13(a). While the multidirectional laminates, CP and QI, exhibit very similar results, the permeability of the UD specimen is notably lower. The stacking sequence has a significant influence on the formation of microcracks and leakage [48,49], however permeability is less affected. As long as the laminates are multidirectional, results appear to be comparable, provided the FVF is comparable. However, in case of a purely UD laminate, permeability is slightly lower. It should be noted, however, that the differences between the CP, QI, and UD laminates fall within the measurement accuracy of the leak detector.

To assess the impact of storage conditions in the laboratory on material properties, samples are stored for 72 h under three different conditions: in an oven at 50 °C (Dry), under ambient conditions (Ambient), and in distilled water (Wet). The results for both measured parameters are presented in Fig. 13(b). Permeability slightly decreases after both dry and wet conditioning compared to ambient storage. The mean helium flux values are 2.10, 2.22, and 1.93 $\left[10^{-4}\,\frac{mbar \cdot l}{s \cdot m^2}\right]$ for dry, ambient, and wet conditions, respectively. While the wet-conditioned samples exhibit the lowest permeability, the difference relative to ambient storage is approximately 13%, which falls within the measurement uncertainty of the leak detector of ±15%. Furthermore, if permeability were affected by conditioning, permeability under dry conditions should be highest and decreasing with ambient and wet conditions, as moisture represents an obstacle for the helium molecules. However, this is not the case in Fig. 13(b). Thus, it is concluded that the results do not indicate a significant influence of conditioning on permeability. It should be noted that these ageing protocols represent laboratory storage conditions prior to permeability testing, rather than the conditions experienced by a tank during service.

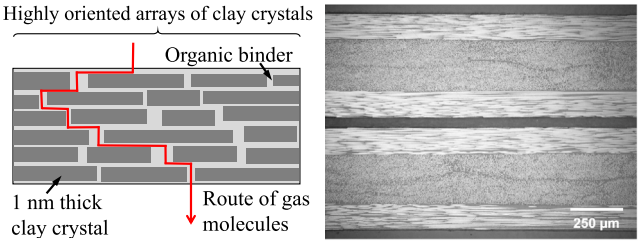

(a) CBF structure [36] (b) Microsection

Fig. 14. Schematic representation of the CBF micro-structure and barrier working principle (left) and microsection of one layer of CBF laminated into a CFRP specimen (right).

4.1.5. Potential of barrier materials

Permeability under cryogenic conditions is less of a problem for insulation design due to the reduced molecule mobility, and the thereby resulting low molecule flux. However, during filling and cooling of the tank, higher temperatures lead to an increase in permeability which in turn can affect the insulation efficiency. While metals come with a large weight penalty in terms of permeation barrier, another material class can potentially help reduce permeability at minimal structural weight increase. Clay-based film (CBF) is a flexible film material developed by the National Institute of Advanced Industrial Science and Technology (AIST). It is composed mainly of clay with a small amount of organic binder. CBF was initially designed as a gas barrier for high-temperature environments where conventional materials fail. However, its capabilities promise useful at cryogenic conditions as well. It is produced by laminating platelet-shaped clay crystals (each 1 nm thick) in a highly oriented structure [50], ensuring its barrier effectiveness (cf. Fig. 14). By effectively reducing the net cross-section for molecule transport and increasing the path of each molecule, permeability is effectively decreased [36]. Its application as a gas barrier for hydrogen pressure vessels has previously been investigated showing high elongation at break and gas barrier properties [51].

Fig. 15 demonstrates the potential of CBF as a barrier material. A reference CFRP specimen with a thickness of 1 mm and a CP layup $[0,90_2,0]_s$ is tested at a pressure of 5 bar. For comparison, a specimen with the same layup but one layer of CBF (60 µm in thickness and a clay/binder content of 70%/30% provided by Kunimine Ind.) in the mid-plane of the laminate ($[0,90_2,0,\underline{CBF}]_s$) is tested under identical test conditions. Specimen manufacturing is identical to the monolithic CFRP specimen, with one additional step in which the CBF, with a sheet size of roughly 200 × 300 mm was cut to size (150 × 200 mm) and laminated into the CFRP layup. No additional surface preparation is needed. The specimens for permeability testing, with a diameter of 55 mm, were milled after curing of the laminate.

Two key effects are observed: First, CBF reduces diffusivity, delaying the onset of helium flux detection from approximately 1 h to over 38 h. Additionally, steady-state conditions take significantly longer to reach with CBF (≈270 h) compared to monolithic CFRP (≈19 h). Second, at steady state, the helium flux is reduced by a factor of 83. While significant, literature on CBF suggests that permeability reductions of up to 500–1000 times is possible [36]. For practical applications, the reduced diffusivity is particularly promising for maintaining vacuum levels in hydrogen tanks during non-cryogenic operation.

Current challenges with CBF primarily concern its adhesion to CFRP. Ultrasound scanning was conducted on the specimens using a pulser/receiver setup with a 5 MHz head (USPC 3010 VHF by Hildinger NDT). As shown in Fig. 16, the material combination is prone to delamination from the CFRP plies. However, this issue can be mitigated by increasing the binder-to-clay ratio, which enhances adhesion and reduces the risk of delamination. In general, CBF shows good adhesion to CFRP based on investigations where neither cryogenic cycling in

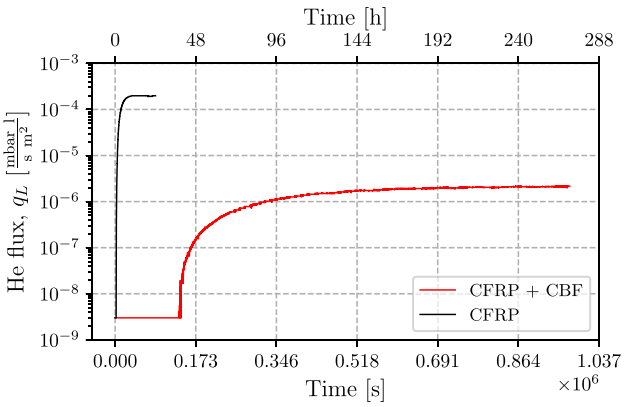

Fig. 15. Helium flux in reference CFRP specimen and CFRP specimen with one CBF layer of 60 µm in thickness.

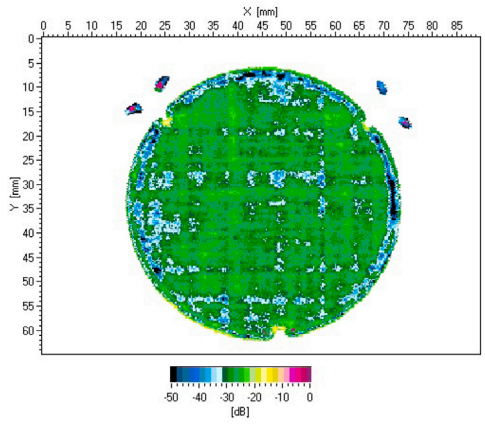

(a) Reference CFRP specimen

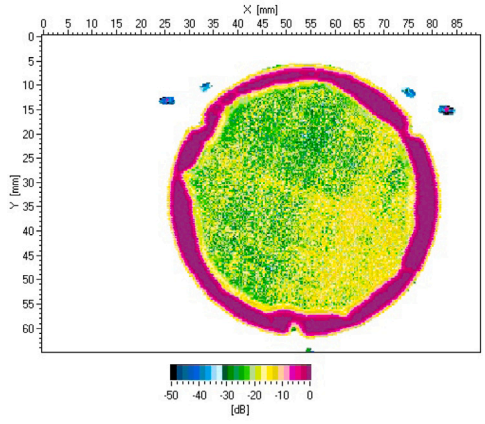

(b) CFRP with CBF

Fig. 16. Ultrasound C-scans of permeability specimens.

liquid nitrogen nor 10,000 load cycles to 5,000 $\mu\varepsilon$ lead to degradation of the gas barrier properties [36]. However, quantification of the interlaminar fracture toughness of the interface between CBF and CFRP by means of double-cantilever beam and end-notched flexure testing specifically at low temperature will be necessary in the future to quantify the compatibility between CBF and CFRP. Future work should include an increased number of specimens to enable statistical assessment of barrier performance. Additionally, it should be noted that the current observations are based on specimens made in a hand-layup process using an autoclave. Effectiveness of the CBF barrier properties and mechanical compatibility with industrial manufacturing processes, e.g. automated fiber placement, need to be verified in the future to further drive the technology towards application in cryogenic tanks.

4.2. Permeability at cryogenic temperature

Low temperature and cryogenic testing is conducted using the permeability setups CIPT and CVPT in Fig. 10. For all cases, a CFRP specimen with CP layup and 1 mm thickness is tested at 5 bar pressure.

4.2.1. Limitations of cryogenic permeability testing

Permeability testing at cryogenic temperatures presents significant challenges. The temperature dependence of permeability follows the Arrhenius relation, which states that the permeation rate increases exponentially with temperature. This relationship is mathematically expressed as

$$P = P_0 \cdot \exp\left(\frac{-E_a}{R_m T}\right) \tag{3}$$

where P is the permeability, P_0 is the permeability as $T \to \infty$, E_a is the activation energy, R_m is the universal gas constant, and T is the temperature. This expression is widely applied to describe thermally activated processes, such as chemical reactions and diffusion phenomena. At very low temperatures, the detection capabilities of state-of-the-art leak detectors (e.g., ASM 340 by Pfeiffer Vacuum GmbH) are fundamentally limited. This threshold is already reached at 77 K in the present case. Increasing the surface area for permeability testing likely is ineffective, as the resulting gain would be insufficient to compensate for the orders-of-magnitude reduction in detectable permeation rates. Consequently, alternative testing strategies are required. Fig. 18 illustrates the temperature dependence of permeability and the limitations of current testing setups.

4.2.2. Low temperature testing approach

Instead of testing inside a LN_2 bath at 77 K, permeability testing is conducted in cold nitrogen gas. This way, permeability values at temperatures below RT can be determined. In the following a 3-step approach is presented for estimating permeability at cryogenic temperatures beyond current detection limits.

Step 1: Experimental permeability testing at different temperatures

Step 2: Determining a regression curve based on the experimental permeability test results using the Arrhenius relation

Step 3: Extrapolation of permeability values for any given temperature

In Step 1, testing at different testing temperatures is conducted. The goal is to produce a sufficient number of data points across a relatively large temperature interval for the subsequent regression. While RT testing is done in the MSPT setup (cf. Fig. 7), testing at elevated temperature (81 °C) is conducted by placing the specimen holder in an industrial oven, and low temperature testing (−34 °C and −54 °C) is done in the CVPT setup (cf. Fig. 10(b)). Fig. 17 presents the test results at −34 °C. In the CVPT setup, temperature control is achieved indirectly by adjusting the LN_2 fill level. Each refill cycle, visible in the test data, introduces vapor phase mixing, which influences the measured helium flux. Since both pressure and permeability are temperature-dependent, this effect must be accounted for. To mitigate the variability introduced by this cooling method, a regression on the helium flux q_L is performed using Fick's law (see Eq. (4)):

$$J(t) = J_{ss}\left[1 + 2\sum_{n=1}^{100}(-1)^n \exp\left(\frac{-Dn^2\pi^2}{d^2}t\right)\right] \tag{4}$$

The steady-state molecular flux J_{ss} and the diffusivity D are fitted. Taking the mean temperature during testing and the relation $q_{L,ss} = J_{ss}RT$ [14], permeability values are calculated using Eq. (1) (see Table 1). While regression based on Fick's law is applied to determine

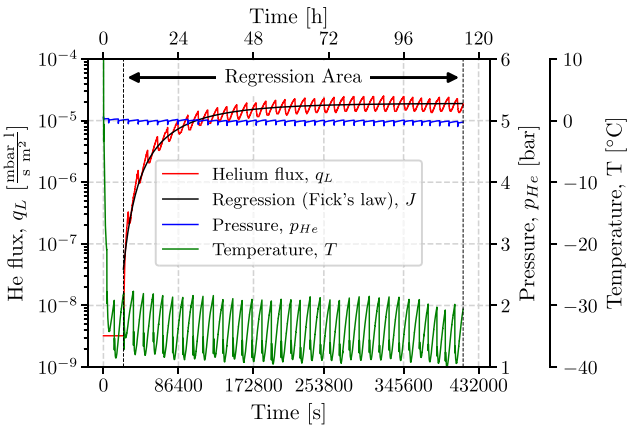

Fig. 17. Permeability of a CFRP specimen at -34 ± 3 °C.

Table 1
Results of permeability testing of CFRP specimen at varying temperatures.

T [°C]	q_L [mbar l / s m²]	P [mol / s m Pa]	D [m² / s]	t_{ss} [h]
−53.75 ± 4.11	$8.80 \cdot 10^{-6}$	$7.26 \cdot 10^{-19}$	$5.66 \cdot 10^{-13}$	236
−34.25 ± 3.32	$1.86 \cdot 10^{-5}$	$1.53 \cdot 10^{-18}$	$1.35 \cdot 10^{-12}$	115
22.56 ± 0.54	$2.22 \cdot 10^{-4}$	$1.81 \cdot 10^{-17}$	$1.14 \cdot 10^{-11}$	26
81.20 ± 0.22	$1.01 \cdot 10^{-3}$	$8.31 \cdot 10^{-17}$	$4.93 \cdot 10^{-11}$	8.5

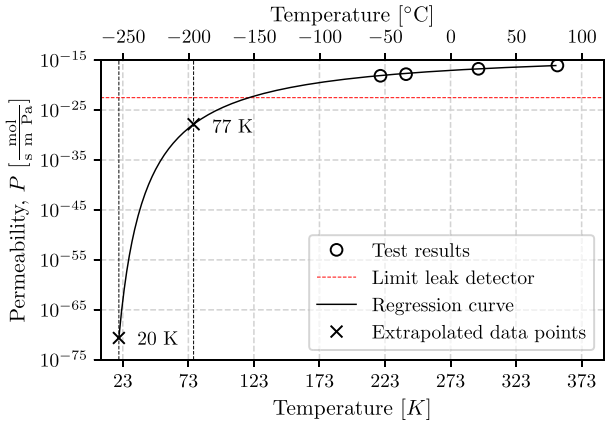

Fig. 18. Temperature dependency of permeability in CFRP.

permeability for the low temperature tests due to temperature induced oscillation, the steady-state values at RT and 81 °C can be read directly from the test data. During testing at 81 °C, it only takes about 8.5 h until steady-state conditions are reached, while testing at −54 °C requires a testing time of at least 236 h until the plateau is reached. It should be noted that another test at −97.4 °C was cancelled after 228 h as no change in helium flux was observed. By estimation based on Eq. (3) and Eq. (4) it would take around 4400 h or 183 days until steady-state conditions are reached. Thus, in order to increase data points, testing at higher temperatures is recommended as this also decreases testing time.

In Step 2, the test results from the previous step are taken as input data for yet another regression (see Fig. 18). In this case, the permeability P at the four temperatures between −54 °C and 81 °C are plotted. As can be seen, testing at −54 °C is already approaching the limit of the leak detector for the present case. Based on those four data points, a regression is performed using the Arrhenius relation in Eq. (3) and the regression curve is plotted in Fig. 18.

In Step 3, the regression based on the Arrhenius relation is used to estimate permeability at 77 K (−196 °C) and 20 K (−253 °C), see also Table 2. As permeability values of CFRP at cryogenic conditions are extremely rare, verification by comparison to other literature is difficult. However, the result of the regression provides the value for permeability P_0 as $T \rightarrow \infty$. In the present case, this value is $1.519 \cdot 10^{-13} \frac{\text{mol}}{\text{s m·Pa}}$, which seems reasonable compared to values for CFRP from literature that range between 10^{-13}...10^{-14} [14]. However, experimental values at cryogenic temperature, e.g. from large scale cryogenic tank tests, are necessary to validate the approach and quantify its accuracy for cryogenic temperatures. It should be noted that extrapolation of permeability represents a regression-based engineering estimate and is only valid for pristine material with Fickian or near-Fickian behavior. The extrapolated values should therefore be interpreted as order-of-magnitude lower-bound estimates for preliminary design considerations rather than predictive material constants. Experimental validation requires substantially larger permeation areas and remains subject of ongoing work. Extrapolation of the helium flux through damaged specimen with micro-crack networks based on the 3-step approach is not possible.

Table 2
Extrapolated permeability and diffusivity values for CFRP specimen.

T [°C]	P [mol / s m Pa]	D [m² / s]
−196 (77 K)	$1.46 \cdot 10^{-28}$	$2.78 \cdot 10^{-22}$
−253 (20 K)	$2.33 \cdot 10^{-71}$	$3.09 \cdot 10^{-63}$

4.3. Effects of microcracks on permeability and leakage

In the previous section, the effects of testing conditions on permeability in pristine CFRP material was investigated. In the following, the focus is put upon damaged laminates. A variety of loading conditions, spanning thermal, mechanical, and combined thermo-mechanical loading as well as uni- and biaxial loading, is considered in an attempt build an understanding of the transition from permeability to leakage in composites. Crack densities were determined from 20 mm wide sections taken from the center of the specimens in both longitudinal and transverse directions, enabling assessment of crack occurrence in all laminate orientations by optical microscopy using Keyence VHX-7000 microscope.

4.3.1. Thermal cycling and uniaxial mechanical loading

The literature reveals conflicting findings regarding the impact of thermal and mechanical loads. While some studies report leakage following thermal cycling [17–19], others show that specimens remain leak-tight [12–14]. Fig. 19 illustrates the relationship between crack density and permeability for CFRP specimens fabricated from 8552/IM7 with a layup of $[45_2, -45_2, 90_2, 0_2]_s$. Block stacking and an angle offset of 90° is applied to increase the tendency for crack formation. All specimens are 70 mm wide and 260 mm long. Each data point represents the average of three specimens. Within the study, some specimens underwent only thermal loading by immersion in LN_2 (1, 2, or 10 cycles), while others were subjected solely to mechanical loading, with tensile strains of 0.4% (approaching the transverse failure strain of a UD laminate) and 0.8% (to induce cracking in the transverse plies). A third group experienced combined thermal and mechanical loading. After their respective loading histories, specimens were tested for permeability at room temperature and 5 bar using the MSPT setup. The aim is to isolate the thermal and mechanical contributions to microcrack formation.

Thermal loading introduces microcracks into the laminate. Although a single LN_2 cycle produces few cracks, multiple cycles (two or more) significantly increase crack density. As shown in Fig. 20(b), thermally induced cracks typically initiate in the surface plies and propagate towards the laminate's center. Despite the increased crack density, the

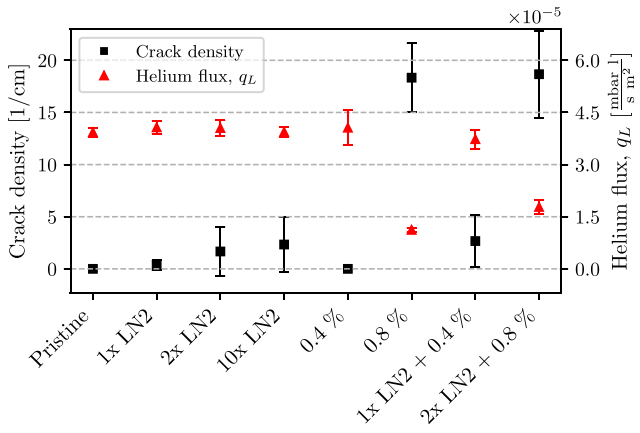

Fig. 19. Crack density of thermally, mechanically, and thermo-mechanically loaded specimen with a QI layup of $[45_2,-45_2,90_2,0_2]_s$.

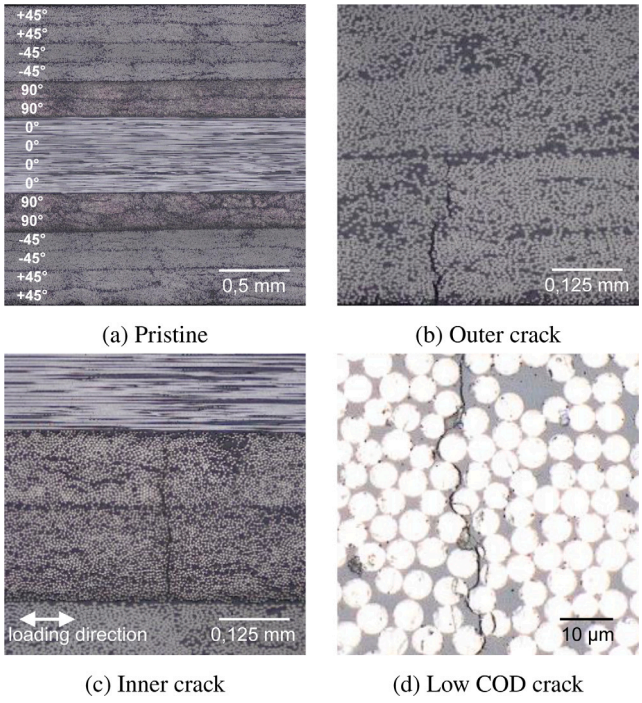

Fig. 20. Microsections of pristine specimen and examples of a thermally induced transverse crack (outer crack), a mechanically induced transverse crack (inner crack) at 0.8%, and a crack with low COD.

helium flux remains similar to that of pristine material, indicating that the transport mechanism remains diffusion-driven (i.e., permeability-dominated).

Pure mechanical loading: Under uniaxial tensile loading to 0.4% strain, no significant microcrack formation is observed, despite reaching near the transverse failure strain for 8552/IM7 (≈0.4–0.6%). This is attributed to the in-situ effect that inhibits crack development in the 90° plies [52]. In contrast, loading to 0.8% strain induces a notable increase in crack density. As opposed to the case of pure thermal loading, where cracks are induced in the outer plies, mechanical loading mainly introduces cracks in the 90° plies inside the laminate, as can be seen in Fig. 20(c). Permeability testing of the material shows values comparable to the pristine material for the specimens that are loaded to 0.4% tensile strain. The specimens that are loaded to 0.8% tensile strain surprisingly show a decrease in permeability. Observation of the laminates under the microscope post permeability testing does not

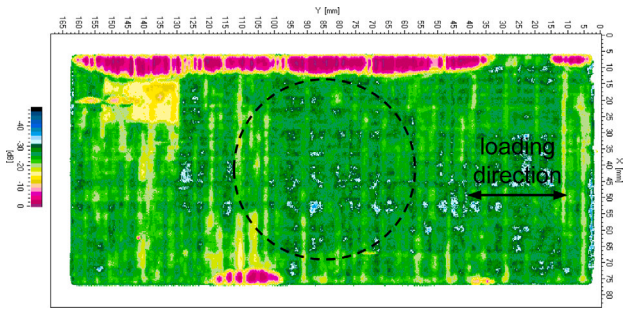

Fig. 21. Ultrasound C-scan of specimen loaded to 0.8% (area of permeability measurement marked by black dashed line).

reveal any crack networks. Rather, it is assumed that the combination of edge delaminations and transverse cracks affect permeability testing. As can be seen in the C-scan image of one of the specimens that is loaded to 0.8% tensile strain in Fig. 21, edge delaminations coupled with transverse cracks create alternative flow paths to the sides of the specimen that interfere with the 1D helium flux and affect the permeability measurement.

Combined thermo-mechanical loading: Alternating thermal cycling and mechanical loading indicates that the loading history affects the formation of microcracks. While neither pure thermal loading (1x LN_2 cycle) nor pure mechanical loading (0.4% strain) significantly affects crack density, applying 0.4% strain after an LN_2 immersion leads to an increase in crack density. It appears that initial microcracks from thermal cycling are enlarged by subsequent mechanical loading. Increasing the thermo-mechanical load to 2 LN_2 cycles followed by 0.8% strain yields crack density and permeability results comparable to pure mechanical loading at 0.8% strain. It should be noted that while most cracks exhibit a crack opening displacement (COD) of around 5–10 µm,consistent with literature reports [53], some few cracks with significantly lower COD were observed in the specimens that were exposed to both thermal and mechanical loading. As can be seen in Fig. 20(d), these cracks exhibit a COD of below 1 µm which makes them difficult to detect during analysis. Accurate determination of crack density therefore requires high magnification during analysis, since these cracks can be potentially overlooked otherwise. This observation is particularly important for future efforts in non-destructive inspection (NDI) of CFRP structures, as defects of this size can be difficult to detect using state-of-the-art methods, such as ultrasonic scanning.

Notably, none of the specimens in this study exhibit a continuous crack network spanning the laminate thickness. Since mechanical loading remains the primary driver of crack formation, multi-axial loading appears necessary to induce cracks across all plies, ultimately leading to leakage. Additionally, as cryogenic cooling increases matrix brittleness [54–57], biaxial loading under cryogenic temperatures is the most likely scenario to generate a through-thickness crack network. Considering the development of hydrogen tanks, it is concluded that uniaxial loading is neither representative of the loading cases inside the tank nor does uniaxial loading exhibit conservatism regarding crack formation.

4.3.2. *Biaxial mechanical loading*

As concluded in the previous section, unidirectional loading alone does not result in the formation of a crack network in multidirectional laminates. Thus, in the present section results are presented for a CFRP specimen with a $[45_2/-45_2]_s$ stacking sequence that is loaded biaxially at room temperature. Again, block stacking is applied to increase the tendency for crack formation. The specimen is loaded biaxially, by step-wise increasing the loads (ratio 1:1) to 45 kN, 60 kN, 65 kN, and 68.8 kN, equal to a biaxial strain state of 0.15%, 0.20%, 0.21%, and 0.22%, respectively. In between the loading steps, the damage state

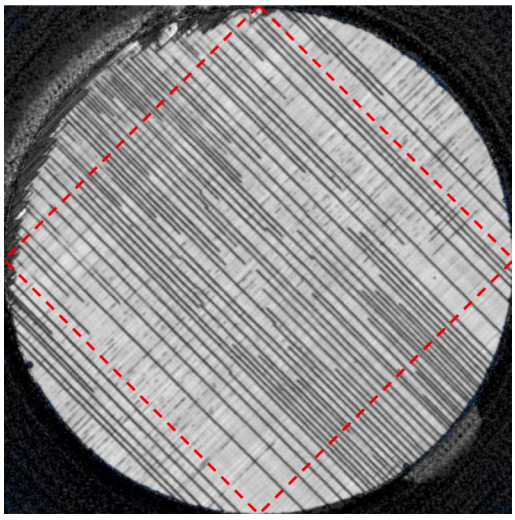

Fig. 22. Ultrasound scan of center area of cruciform specimen after loading to $\epsilon_x = \epsilon_y = 0.22\%$ at JAXA. Red dashed line marks the area (70 × 70 mm) that is cut out for subsequent leakage testing at DLR.

of the specimen is analyzed using ultrasonic C-scan to monitor matrix crack growth in CFRP laminates after each loading step. A 25 MHz transducer transmits ultrasound through the specimen, which reflects off a glass plate and returns for detection. This method proved highly sensitive to matrix cracks and was validated against X-ray photography, confirming its effectiveness for CFRP damage detection [45]. The damage state after application of 0.22% is presented in Fig. 22. After the final loading step, the center part of the cruciform specimen is cut and tested in the permeability setups at RT and low temperature.

Prior to testing of the damaged specimen, a pristine specimen of the same material (HTA/#101) is tested at RT in the MSPT setup and exhibits a permeability P of $2.6{\cdot}10^{-17}\,\frac{\text{mol}}{\text{s m Pa}}$ $\left(q_L = 3.3\ 10^{-4}\,\frac{\text{mbar l}}{\text{s m}^2}\right)$, which is only slightly lower than in the case of 8552/IM7. It should be noted that the biaxial experiments were conducted using a different material system and layup than the uniaxial and thermal investigations. Consequently, the following discussion focuses on qualitative trends and underlying mechanisms rather than a direct quantitative comparison. The result of the pristine specimen serves as a reference for the damaged specimen, which is tested next. In a first step, testing at RT is conducted (cf. Fig. 23). Starting at an absolute pressure of 0.96 bar, the value is increased to 1.57 bar in two steps (cf. Fig. 23). At this point, due to the high leakage through the CFRP specimen, the leak detector reaches its upper limit beyond which measurement will significantly pollute the mass spectometer inside the detector and prevent further testing. This is why the pressure is not further increased. In order to get more data points, a finer pressure reducer is used for subsequent testing. A range between 0.21 bar to 0.86 bar absolute pressure is tested. The slope of the helium leakage at pressures below 1 bar is steeper, compared to testing at pressures above 1 bar. As both pressure reducers have the same working principle, it is assumed that this change in slope is in fact a non-linear dependency of leakage on the applied pressure. A possible explanation is choking of the helium flow at higher pressures. At lower pressures (< 1 bar), the flow remains subsonic, and the leakage rate scales more directly with the pressure [58]. In this regime, the flow resistance of the crack network primarily governs the leakage rate. However, at higher pressures (> 1 bar), the flow within the microchannels of the CFRP specimen may begin transitioning into choked conditions. Once the flow becomes choked, increasing the upstream pressure further has little effect on the mass flow, which could explain the observed flattening of the leakage rate curve at higher pressures [59]. However, more testing on this topic is necessary for a definitive explanation on this phenomenon.

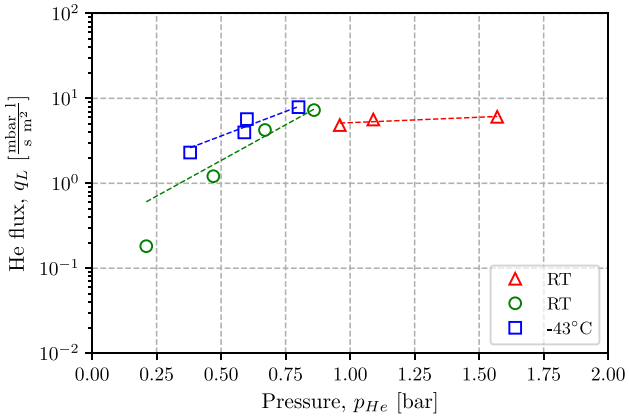

Fig. 23. Leak rates in CFRP specimen at varying pressure and temperature after biaxial loading to $\epsilon_x = \epsilon_y = 0.22\%$.

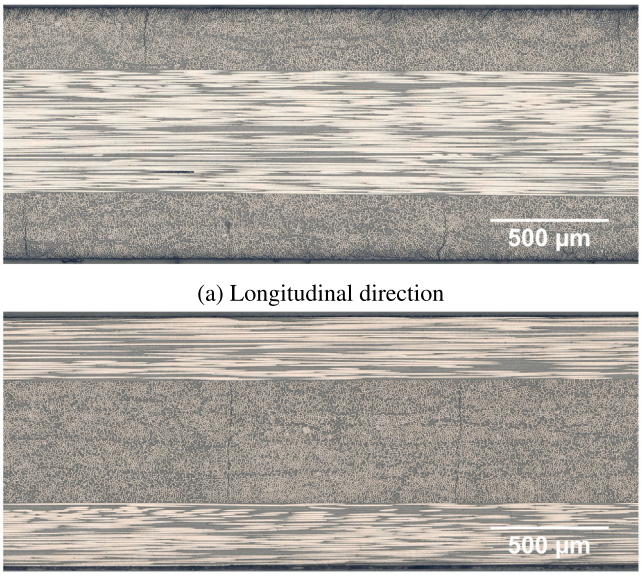

(a) Longitudinal direction

(b) Transverse direction

Fig. 24. Microsections of the center area of the specimen after biaxial loading to $\epsilon_x = \epsilon_y = 0.22\%$.

Using the CVPT setup, leakage tests were conducted at -43 ± 5 °C. As shown in Fig. 23, the leakage exhibits a pronounced dependence on temperature, with increasing leakage towards lower temperatures at pressures below 1 bar. A direct causal attribution of this behavior to temperature-dependent COD cannot be established based on the present measurements, as no in-situ characterization of crack geometry was performed. However, both experimental [37,60] and numerical [61,62] studies reported in the literature indicate that decreasing temperature can increase internal thermal residual stresses in CFRP, which may influence microcrack evolution and COD. Consequently, leakage-dominated transport is expected to exhibit sensitivity to the crack network geometry at low temperature. Further testing in the CIPT at −196 °C (77 K) was conducted. However, leakage through the specimen was so large that the maximum inlet pressure for the leak detector was again exceeded, preventing testing at cryogenic conditions. Nonetheless, it could be shown that biaxial loading effectively introduces crack networks into CFRP specimens at strain levels well below what was expected considering crack initiation in the unidirectional tests in Section 4.3.1, despite the difference in material and layup.

After completing the leakage tests, the specimens were sectioned to obtain micrographs. Fig. 24 shows cross-sections in both the longitudinal and transverse directions of a damaged specimen. The crack densities in the outer and inner plies are comparable, with the outer layers exhibiting a crack density of $4.9 \pm 0.4\,\mathrm{cm}^{-1}$ and the center ply showing $4.8 \pm 0.8\,\mathrm{cm}^{-1}$. As shown, cracks extend across the entire width of all ply stacks, suggesting the presence of an interconnected crack network. However, no delamination is observed connecting individual microcracks. Instead, the micrographs suggest that the crack network forms through discrete intersections of microcracks in adjacent plies. Although no direct three-dimensional microstructural visualization of crack connectivity is available, the combination of a high ply-wise crack density observed in longitudinal and transverse microsections and the occurrence of measurable leakage during pressurization provides strong indirect evidence for the presence of a connected crack network.

5. Conclusions

This paper aims to provide a comprehensive understanding of the peculiarities of hydrogen tank development in terms of permeability and leakage.

Regarding diffusion based molecular flux, i.e. permeability, the paper provides experimental values for helium and hydrogen permeability for HDPE, thereby adding observations on the seldom addressed topic of the comparability of these two tracer gases. Also, the effects of testing parameters and specimen configuration on test results are investigated, and recommendations for pragmatic permeability testing are given. In particular, a pragmatic approach to estimate permeability values at cryogenic temperatures is presented, allowing to approximate permeability values for very low temperatures where the limitations of state-of-the-art testing devices are reached. Furthermore, it is shown that CBF – a potential barrier material – can reduce permeability for certain critical conditions during transient operation of a CFRP liquid hydrogen tank. Future work should focus on advancing experimental methods capable of directly resolving very low permeability values at cryogenic temperatures.

In addition, fluid flow based molecular flux, i.e. leakage, is investigated. Isolated as well as combined thermo-mechanical loading reveal different characteristics on microcrack formation depending on the loading history. Furthermore, it is shown that uniaxial loading generally induces microcracks in a preferred orientation (transverse to the loading direction), which does not lead to the formation of microcrack networks and leakage. Biaxial loading on the other hand leads to microcracks in all plies of a laminate resulting in leakage through microcrack networks, with the molecular flux during testing being both temperature- and pressure-dependent. Thus, the biaxial experiments indicate that multi-axial stress states are a key prerequisite for the formation of through-thickness crack networks and leakage in CFRP. However, it should be noted that uniaxial and biaxial testing were conducted with different CFRP materials, therefore conclusions are qualitative in nature and focus on the underlying mechanisms and loading conditions of crack network formation rather than a direct quantitative comparison between specific strain levels. Future work will further focus on increasing the number of replicates to enable statistical assessment.

Together, the results provide an experimental basis for understanding the interplay between permeability, microcracking, and leakage under varying conditions, and support the development of design strategies for cryogenic CFRP hydrogen tanks.

CRediT authorship contribution statement

J. Koord: Writing – review & editing, Writing – original draft, Visualization, Validation, Software, Methodology, Investigation, Formal analysis, Data curation, Conceptualization. **H. Kumazawa:** Writing – review & editing, Visualization, Validation, Resources, Methodology, Investigation, Formal analysis, Data curation, Conceptualization. **A. Fischer:** Writing – review & editing, Visualization, Validation, Methodology, Investigation, Formal analysis, Data curation, Conceptualization. **T. Ebina:** Writing – review & editing, Visualization, Resources, Investigation, Data curation, Conceptualization. **O. Völkerink:** Writing – review & editing, Resources, Project administration, Conceptualization. **C. Hühne:** Writing – review & editing, Supervision, Resources, Project administration, Funding acquisition, Conceptualization.

Declaration of competing interest

The authors declare that they have no known competing financial interests or personal relationships that could have appeared to influence the work reported in this paper.

Acknowledgments

The authors would like to acknowledge funding from German Aerospace Center (DLR) within the initiative ACTION — Advanced Cryogenic Technologies and Simulation. The authors further would like to thank Kunimine Industries Co., Ltd. for providing the CBF sheets that were investigated in this study.

Data availability

Data will be made available on request.

References

[1] Hoelzen J, Silberhorn D, Zill T, Bensmann B, Hanke-Rauschenbach R. Hydrogen-powered aviation and its reliance on green hydrogen infrastructure – Review and research gaps. Int J Hydrog Energy 2022;47(5):3108–30. http://dx.doi.org/10.1016/j.ijhydene.2021.10.239.

[2] Degirmenci H, Uludag A, Ekici S, Karakoc TH. Challenges, prospects and potential future orientation of hydrogen aviation and the airport hydrogen supply network: A state-of-art review. Prog Aerosp Sci 2023;141:100923. http://dx.doi.org/10.1016/j.paerosci.2023.100923.

[3] Mukwanje CA, Faik A, Nachtane M. Current progress, challenges, and future prospects in composite cryogenic hydrogen storage tanks. Polym Compos 2025;46(S2). http://dx.doi.org/10.1002/pc.29872.

[4] Silberhorn D, Dahlmann K, Görtz A, Linke F, Zanger J, Rauch B, Methling T, Janzer C, Hartmann J. Climate impact reduction potentials of synthetic kerosene and green hydrogen powered mid-range aircraft concepts. Appl Sci 2022;12(12):5950. http://dx.doi.org/10.3390/app12125950.

[5] Burschyk T, Cabac Y, Silberhorn D, Boden B, Nagel B. Liquid hydrogen storage design trades for a short-range aircraft concept. CEAS Aeronaut J 2023;14(4):879–93. http://dx.doi.org/10.1007/s13272-023-00689-4.

[6] Hoff T, Becker F, Dadashi A, Wicke K, Wende G. Implementation of fuel cells in aviation from a maintenance, repair and overhaul perspective. Aerospace 2022;10(1):23. http://dx.doi.org/10.3390/aerospace10010023.

[7] Gomez A, Smith H. Liquid hydrogen fuel tanks for commercial aviation: Structural sizing and stress analysis. Aerosp Sci Technol 2019;95:105438. http://dx.doi.org/10.1016/j.ast.2019.105438.

[8] Zheng H, Zeng X, Zhang J, Sun H. The application of carbon fiber composites in cryotank. In: Solidification. InTech; 2018, http://dx.doi.org/10.5772/intechopen.73127.

[9] Mital S, Gyekenyesi JZ, Arnold SM, Sullivan RM, Manderscheid JM, Murthy PL. Review of current state of the art and key DesignIssues with potential solutions for liquid HydrogenCryogenic storage tank structures for AircraftApplications. 2006, Tm—2006-214346 NASA.

[10] Niedermeyer M. X-33 LH2 tank failure investigation findings. In: International conference on composites engineering. NASA Marshall Space Flight Center; 2003.

[11] Bordekar H, Koord J, Völkerink O, Hühne C. Microstructure characterization of fiber composite laminate using explainable artificial intelligence. J Compos Mater 2025;60(1):3–25. http://dx.doi.org/10.1177/00219983251345559.

[12] Disdier S, Rey J, Pailler P, Bunsell A. Helium permeation in composite materials for cryogenic application. Cryogenics 1998;38(1):135–42. http://dx.doi.org/10.1016/s0011-2275(97)00124-0.

[13] Humpenöder J. Gas permeation of fibre reinforced plastics. Cryogenics 1998;38(1):143–7. http://dx.doi.org/10.1016/s0011-2275(97)00125-2.

[14] Schultheiß D. Permeation barrier for lightweight liquid hydrogen tanks [Ph.D. thesis], Universität Augsburg; 2007.

[15] Kessler SS, Matuszeski T, McManus H. Cryocycling and mechanical testing of CFRP for X-33 liquid H2 fuel tank structure. In: 16th ASC technical conference. 2001.

[16] Bogenfeld R, Lüders C, Ebermann M, Ravi V. A direct correlation between damage parameters and effective permeation coefficients in composite laminates. Compos Part A: Appl Sci Manuf 2024;185:108307. http://dx.doi.org/10.1016/j.compositesa.2024.108307.

[17] Bechel V. Permeability and damage in unloaded cryogenically cycled PMCs. In: 46th AIAA/aSME/ASCE/AHS/aSC structures, structural dynamics and materials conference. American Institute of Aeronautics and Astronautics; 2005, http://dx.doi.org/10.2514/6.2005-2156.

[18] Choi S, Sankar BV. Gas permeability of various graphite/epoxy composite laminates for cryogenic storage systems. Compos Part B: Eng 2008;39(5):782–91. http://dx.doi.org/10.1016/j.compositesb.2007.10.010.

[19] Flanagan M, Grogan D, Goggins J, Appel S, Doyle K, Leen S, Ó Brádaigh C. Permeability of carbon fibre PEEK composites for cryogenic storage tanks of future space launchers. Compos Part A: Appl Sci Manuf 2017;101:173–84. http://dx.doi.org/10.1016/j.compositesa.2017.06.013.

[20] Just T, Will J, Haberstroh C. Hydrogen permeabilty testing of fibre reinforced thermoplastics under cryogenic conditions – a test rig concept.. In: Cryogenics 2023. proceedings of the 17th IIR international conference, dresden, Germany, April 25-28 2023. International Institute of Refrigeration (IIR); 2023, http://dx.doi.org/10.18462/IIR.CRYO.2023.0149.

[21] Just T, Will J, Haberstroh C. Hydrogen permeability testing of fibre reinforced thermoplastics under cryogenic conditions – validation of a test rig concept. IOP Conf Ser: Mater Sci Eng 2024;1301(1):012063. http://dx.doi.org/10.1088/1757-899x/1301/1/012063.

[22] Humpenöder J. Gaspermeation von faserverbunden mit polymermatrices [Ph.D. thesis], Karlruhe Institute of Technology; 1997.

[23] Hohe J, Neubrand A, Fliegener S, Beckmann C, Schober M, Weiss K-P, Appel S. Performance of fiber reinforced materials under cryogenic conditions—A review. Compos Part A: Appl Sci Manuf 2021;141:106226. http://dx.doi.org/10.1016/j.compositesa.2020.106226.

[24] Saha S, Sullivan RW. A review on gas permeability of polymer matrix composites for cryogenic applications. J Compos Mater 2024;58(6):827–47. http://dx.doi.org/10.1177/00219983241228550.

[25] Katsivalis I, Signorini V, Ohlsson F, Langhammer C, Minelli M, Asp LE. Hydrogen permeability of thin-ply composites after mechanical loading. Compos Part A: Appl Sci Manuf 2024;176:107867. http://dx.doi.org/10.1016/j.compositesa.2023.107867.

[26] Appels J, Sämann P, Naumann J, Brauer C, Stefaniak D, Atli-Veltin B, Dransfeld C. Investigation of fiber volume fraction as key parameter in cryogenic hydrogen tank development. In: SAMPE 2025 technical proceedings. SAMPE 2025, Society for the Advancement of Material and Process Engineering; 2025, http://dx.doi.org/10.33599/nasampe/s.25.0109.

[27] Timmerman JF, Hayes BS, Seferis JC. Nanoclay reinforcement effects on the cryogenic microcracking of carbon fiber/epoxy composites. Compos Sci Technol 2002;62(9):1249–58. http://dx.doi.org/10.1016/s0266-3538(02)00063-5.

[28] van Rooyen L, Karger-Kocsis J, Vorster O, Kock L. Helium gas permeability reduction of epoxy composite coatings by incorporation of glass flakes. J Membr Sci 2013;430:203–10. http://dx.doi.org/10.1016/j.memsci.2012.11.083.

[29] Zhang J, Lei L, Zhou W, Li G, Yan Y, Ni Z. Cryogenic mechanical and hydrogen-barrier properties of carbon fiber composites for type V cryo-compressed hydrogen storage vessels. Compos Commun 2023;43:101733. http://dx.doi.org/10.1016/j.coco.2023.101733.

[30] Su Y, Lv H, Zhou W, Zhang C. Review of the hydrogen permeability of the liner material of type IV on-board hydrogen storage tank. World Electr Veh J 2021;12(3):130. http://dx.doi.org/10.3390/wevj12030130.

[31] Yokozeki T, Aoki T, Ishikawa T. Experimental cryogenic gas leakage through damaged composite laminates for propellant tank application. J Spacecr Rockets 2005;42(2):363–6. http://dx.doi.org/10.2514/1.13955.

[32] Torres A, Soto C, Carmona J, Comesaña-Gandara B, de la Viuda M, Palacio L, Prádanos P, Simorte MT, Sanz I, Muñoz R, Tena A, Hernández A. Gas permeability through polyimides: Unraveling the influence of free volume, intersegmental distance and glass transition temperature. Polymers 2023;16(1):13. http://dx.doi.org/10.3390/polym16010013.

[33] Dreossi G, Horvat AB. Permeation investigation of carbon fibre reinforced polymer material for LH2 storage thermally shocked and mechanically cycled at cryogenic temperature. Aerospace 2025;12(4):342. http://dx.doi.org/10.3390/aerospace12040342.

[34] Bechel VT, Negilski M, James J. Limiting the permeability of composites for cryogenic applications. Compos Sci Technol 2006;66(13):2284–95. http://dx.doi.org/10.1016/j.compscitech.2005.12.003.

[35] Bechel VT, Fredin MB, Donaldson SL, Kim RY, Camping JD. Effect of stacking sequence on micro-cracking in a cryogenically cycled carbon/bismaleimide composite. Compos Part A: Appl Sci Manuf 2003;34(7):663–72. http://dx.doi.org/10.1016/s1359-835x(03)00054-x.

[36] Yonemoto K, Yamamoto Y, Okuyama K, Ebina T. Application of CFRP with high hydrogen gas barrier characteristics to fuel tanks of space transportation system. Trans Japan Soc Aeronaut Space Sci 2009;7(26). http://dx.doi.org/10.2322/tstj.7.pc_13.

[37] Grenoble R, Gates T. Hydrogen permeability of polymer matrix composites at cryogenic temperatures. In: 46th AIAA/aSME/ASCE/AHS/aSC structures, structural dynamics and materials conference. American Institute of Aeronautics and Astronautics; 2005, http://dx.doi.org/10.2514/6.2005-2086.

[38] Ahlborn K. Durability of carbon fibre reinforced plastics with thermoplastic matrices under cyclic mechanical and cyclic thermal loads at cryogenic temperatures. Cryogenics 1991;31(4):257–60. http://dx.doi.org/10.1016/0011-2275(91)90088-e.

[39] Yokozeki T, Ogasawara T, Aoki T, Ishikawa T. Experimental evaluation of gas permeability through damaged composite laminates for cryogenic tank. Compos Sci Technol 2009;69(9):1334–40. http://dx.doi.org/10.1016/j.compscitech.2008.05.019.

[40] Hamori H, Kumazawa H, Higuchi R, Yokozeki T. Numerical and experimental evaluation of the formation of leakage paths through CFRP cross-ply laminates with leak barrier layers. Compos Struct 2019;230:111530. http://dx.doi.org/10.1016/j.compstruct.2019.111530.

[41] Hamori H, Kumazawa H, Higuchi R, Yokozeki T. Gas permeability of CFRP cross-ply laminates with thin-ply barrier layers under cryogenic and biaxial loading conditions. Compos Struct 2020;245:112326. http://dx.doi.org/10.1016/j.compstruct.2020.112326.

[42] Stokes EH. Hydrogen permeability of a polymer based composite tank material under tetra-axial strain. In: 5th conference on aerospace materials, processes, and environmental technology. 2002.

[43] Stokes EH. Hydrogen permeability of polymer based composites underbi-axial strain and cryogenic temperatures. In: 45th AIAA/aSME/ASCE/AHS/aSC structures, structural dynamics and materials conference. AIAA; 2002.

[44] Datasheet 8552/IM7. URL https://www.hexcel.com/user_area/content_media/raw/HexPly_913_eu_DataSheet.pdf.

[45] Kumazawa H, Takatoya T. Damage development and gas leakage in CFRP angle-ply laminates under biaxial loadings. In: American society for composites: twenty-fifth technical conference,dayton, OH. 2010.

[46] Meyer P, Vorhof M, Koord J, Sennewald C, Cherif C, Hühne C. Anisotropic flexure hinges: Manufacturing and mechanical characterization for application in pressure-actuated morphing structures. Compos Part B: Eng 2023;266:110967. http://dx.doi.org/10.1016/j.compositesb.2023.110967.

[47] Flaconneche B, Martin J, Klopffer MH. Permeability, diffusion and solubility of gases in polyethylene, polyamide 11 and poly (vinylidene fluoride). Oil Gas Sci Technol 2001;56(3):261–78. http://dx.doi.org/10.2516/ogst:2001023.

[48] Kumazawa H, Aoki T, Susuki I. Influence of stacking sequence on leakage characteristics through cfrp composite laminates. Compos Sci Technol 2006;66(13):2107–15. http://dx.doi.org/10.1016/j.compscitech.2005.12.017.

[49] Laeuffer H, Guiot B, Wahl J-C, Perry N, Lavelle F, Bois C. Relationship between damage and permeability in liner-less composite tanks :experimental study at the lamina level. In: In: European conference on spacecraft structures,materials and environmental testing, France, 2016-09 - proceedings of the Europeanconference on spacecraft structures, materials and environmental testing - 2016. 2016.

[50] Aizawa T, Kubota M, Ebina T. Temperature dependence of gas barrier property of clay-polymer composite coatings. Appl Clay Sci 2022;226:106571. http://dx.doi.org/10.1016/j.clay.2022.106571.

[51] Ebina T, Ishii R, Aizawa T, Yoshida H. Development of clay-based film and its application to gas barrier layers of composite tanks. J Jpn Pet Inst 2017;60(3):121–6. http://dx.doi.org/10.1627/jpi.60.121.

[52] Camanho PP, Dávila CG, Pinho ST, Iannucci L, Robinson P. Prediction of in situ strengths and matrix cracking in composites under transverse tension and in-plane shear. Compos Part A: Appl Sci Manuf 2006;37(2):165–76. http://dx.doi.org/10.1016/j.compositesa.2005.04.023.

[53] Meng J, Zheng H, Wei Y, Liu D, Shi H, Wang P, Lei H, Fang D. Leakage performance of CFRP laminate under cryogenic temperature: Experimental and simulation study. Compos Sci Technol 2022;226:109550. http://dx.doi.org/10.1016/j.compscitech.2022.109550.

[54] Li Y, Meng J, Niu G, Yang H, Wang P, Lei H, Fang D. Cryogenic damage mechanisms of CFRP laminates based on in-situ X-ray computed tomography characterization. Compos Sci Technol 2024;247:110413. http://dx.doi.org/10.1016/j.compscitech.2023.110413.

[55] Koord J, Hühne C. Effect of low temperature on interlaminar fracture toughness of multi-directional CFRP and CFRP-steel interfaces. Compos Part B: Eng 2024;281:111540. http://dx.doi.org/10.1016/j.compositesb.2024.111540.

[56] Koord J, Hühne C. Bolt-bearing behavior of hybrid CFRP-steel laminates at low temperature. J Compos Mater 2024;58(22):2443–55. http://dx.doi.org/10.1177/00219983241262955.

[57] Dagdag O, Kim H. Cryogenic impact on carbon fiber-reinforced epoxy composites for hydrogen storage vessels. J Compos Sci 2024;8(11):459. http://dx.doi.org/10.3390/jcs8110459.

[58] Dong C, Cui X, Liu S, Jiang Z, Song J, Wu Y, Lu L. Choked flow behavior of helium-4 at cryogenic temperature. Phys Fluids 2022;34(9). http://dx.doi.org/10.1063/5.0105974.

[59] Dong C, Cui X, Liu S, Jiang Z, Wu Y. Investigation on the choked mass-flow characteristics of the helium fluid during the joule-thomson process in micro-orifice under different high pressures. Cryogenics 2022;122:103416. http://dx.doi.org/10.1016/j.cryogenics.2021.103416.

[60] Grogan DM. Damage and permeability in linerless composite cryogenic tanks [Ph.D. thesis], University of Galway; 2015, http://dx.doi.org/10.13025/15908.
[61] Wang P, Bai Y, Li Y, Zhao Z, Duan S, Lei H. A crack density analytical model for multidirectional composite laminates under biaxial stress at cryogenic temperature. Int J Solids Struct 2025;323:113629. http://dx.doi.org/10.1016/j.ijsolstr.2025.113629.
[62] Zhao H, Yuan M, Peng Y, Gao X, Tian L, Zhang B, Zhang C, Chen J. An integrated approach to analyzing matrix-crack-induced stiffness degradation and medium leakage in linerless composite vessels. Compos Part A: Appl Sci Manuf 2024;185:108364. http://dx.doi.org/10.1016/j.compositesa.2024.108364.